

Systematic Analysis of Biomolecular Conformational Ensembles with PENZA

Martin Vögele,^{1,2,3,a)} Neil J. Thomson,⁴ Sang T. Truong,¹ Jasper McAvity,¹ Ulrich Zachariae,⁴ and Ron O. Dror^{1,2,3,5}

¹⁾*Department of Computer Science, Stanford University School of Engineering*

²⁾*Department of Molecular and Cellular Physiology, Stanford University School of Medicine*

³⁾*Department of Structural Biology, Stanford University School of Medicine*

⁴⁾*Division of Computational Biology, School of Life Sciences, University of Dundee*

⁵⁾*Institute for Computational and Mathematical Engineering, Stanford University*

(Dated: 7 December 2022)

Molecular simulations enable the study of biomolecules and their dynamics on an atomistic scale. A common task is to compare several simulation conditions - like mutations or different ligands - to find significant differences and interrelations between them. However, the large amount of data produced for ever larger and more complex systems often renders it difficult to identify the structural features that are relevant for a particular phenomenon. We present a flexible software package named PENZA that enables a comprehensive and thorough investigation into biomolecular conformational ensembles. It provides a wide variety of featurizations and feature transformations that allow for a complete representation of biomolecules like proteins and nucleic acids, including water and ion cavities within the biomolecular structure, thus avoiding bias that would come with manual selection of features. PENZA implements various methods to systematically compare the distributions of these features across ensembles to find the significant differences between them and identify regions of interest. It also includes a novel approach to quantify the state-specific information between two regions of a biomolecule which allows, e.g., the tracing of information flow to identify signaling pathways. PENZA also comes with convenient tools for loading data and visualizing results in ways that make them quick to process and easy to interpret. PENZA is an open-source Python library maintained at <https://github.com/drorlab/pensa> along with an example workflow and a tutorial. Here we demonstrate its usefulness in real-world examples by showing how it helps to determine molecular mechanisms efficiently.

I. INTRODUCTION

Molecules exist not as static structures, but in a range of conformations that fluctuate about energetic equilibria and can be described as a thermodynamic ensemble. In recent years, molecular dynamics (MD) simulations have become one of the standard methods in molecular biology,¹ providing detailed insights into a molecule's conformational ensemble, complementing static experimental structures that represent only the most probable conformation.^{2,3} A common and important problem in molecular biophysics is to probe the effect of two or more similar conditions on a macromolecule and identify the resulting conformational differences and how they relate to each other. Typical analyses include investigating the effects of: small-molecule ligand binding^{4,5}, protein

mutations,⁶ or protonation changes^{7,8}, usually by simulating the macromolecule with and without a particular ligand, mutation, or protonation state. Visual inspection is commonly performed to identify the resulting differences and to derive causal interrelations.^{9,10} However, in systems where the subtleties of a small shift in the populations of minority conformational states or the motion of single atoms might have crucial functional outcomes, analysis is complicated by the large dimensionality of most systems.¹ Even when the dimensionality is distilled to a subset of features, such as torsion angles, simulations contain billions of frames, and functionally relevant differences can extend to regions far from a small-molecule binding site or mutation site.^{1,4,11-14} The necessary analysis is the bottleneck of many molecular biology projects as it can take weeks of dedicated work if performed by eye and by one-off scripts, and a focus on preconceived candidate mechanisms can lead to missing unexpected effects.

In light of these hurdles, the strong interest in ensemble

^{a)}present address: Schrödinger Inc., 1540 Broadway 24th Floor, New York, NY 10036, United States

analyses over the past two decades has led to development of ensemble databases with inbuilt analysis tools¹⁵ and the availability of more powerful, systematic and quantitative approaches, including: single-score similarity measures between two ensembles,^{16,17} implemented in libraries such as Encore¹⁸; generative deep learning methods;¹⁹ Markov model analyses;^{20,21} and neural-network based analyses.^{22,23} For example, DiffNets²³ successfully identified mutation sites that affect the signalling profile of the oxytocin receptor.²⁴ However, the available methods are either computationally costly, difficult to apply, have to be fine-tuned for a particular system, or are not easily interpretable. This shortage of standardized yet flexible analysis tools, specifically for comparison of multiple conditions, poses an obstacle in many research avenues.

We present the modular software library PENSEA²⁵ (short for Python ENSEMBLE Analysis) that enables the flexible implementation of systematic and quantitative yet easily interpretable workflows for exploratory analysis of biomolecular conformational ensembles (Fig. 1). It contains user-friendly tools to preprocess simulation data, to apply various analysis methods across simulation conditions, and to visualize the results. PENSEA is an open-source Python library maintained at <https://github.com/drorlab/pensa> along with an example workflow and a tutorial.

PENSEA reduces the large dimensionality of molecular systems to features that allow for its complete representation (Fig. 2). A typical PENSEA workflow first determines the same features for all ensembles, currently including: amino acid torsions, nucleic acid torsions, arbitrary interatomic distances, and a novel featurization method for water cavities and ion binding sites. The library provides the necessary feature readers and preprocessing tools while allowing for the integration of custom implementations. The ensemble definition is flexible, e.g., the data representing two ensembles could be derived from two independent simulations or from two parts of a single simulation that encompasses two ensembles. Taking into account all features, PENSEA attenuates the bias that would come with manual pre-selection. To further reduce the complexity of a system, classical methods for dimensionality-reduction and clustering can be applied across the joint ensemble combining all conditions, and multiple primary features can be combined to one via multivariate discretization. These features form the basis for the subsequent quantitative analysis that provides a comprehensive insight into the ensembles (Fig. 1).

PENSEA’s analysis methods focus on quantitatively exploring multiple conformational ensembles and discov-

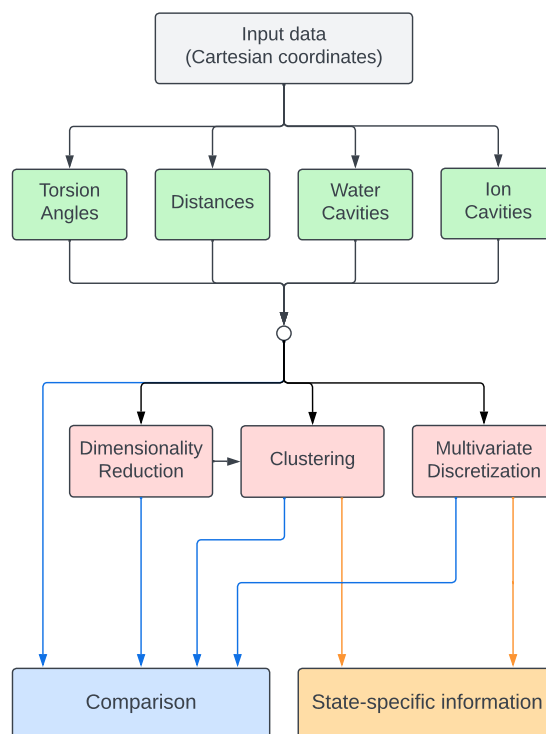


FIG. 1. PENSEA allows a variety of analysis workflows. Green boxes show primary features (section II A) and red boxes show possible feature transformations (section II B). The blue box represents comparison using either the Jensen–Shannon distance (JSD) or the Kolmogorov Smirnov Statistic (KSS), and the yellow box represents the quantification of mutual information using State-Specific Information (SSI) or State-Specific Co-information (CoSSI), which are discussed in sections II C and II D, respectively. PENSEA’s modular nature allows for flexibility in the path from input data to analysis metric.

ering interrelations within and between them. To locate the most relevant differences between two ensembles, PENSEA includes a direct comparison of every feature’s distribution between ensembles via Jensen-Shannon distance (JSD) and the Kolmogorov-Smirnov statistic (KSS). Furthermore, a mutual information analysis based on state-specific information⁸ (SSI), is included to provide a measure of the information that features signal about the ensembles’ conditions or the transitions between them. An extension of SSI to three variables - CoSSI, enables the tracing of information flow between two regions along the intermediary features. While mostly designed with the comparison of two simulation conditions in mind, PENSEA’s analysis methods can be further expanded to more than two ensembles. For an accessible interpretation of the analysis, various visu-

alization options exist that conveniently transfer results to plots, heat maps, or project results onto three dimensional reference structures. With these methods, PENSA makes it easy to perform quantitative and systematic exploratory analyses across multiple conditions for a variety of biomolecular systems.

Here, we discuss the functionality included in PENSA and demonstrate its usefulness on three real-world applications: We show how to describe the influence of local frustration on loop opening during the catalytic cycle of an oxidoreductase²⁸, how to quantify the influence of force-field parameter changes on simulations of nucleic acids²⁹, and how to identify the effect of ionization on receptor proteins. The examples mostly reproduce existing results, confirming the reliability of our approach, but also show additional new discoveries made possible by systematic comparison of molecular simulations.

II. PENSA FUNCTIONALITY

A. Featurization

In general, the 3D structure of a molecule is represented with Cartesian coordinates, but in molecular dynamics, this representation is mostly redundant due to bonded and non-bonded atomic constraints. Other representations summarise the motion of multiple atomic coordinates in a succinct and instructive manner. In the following, we use the term *feature* for every such numerical attribute calculated from the coordinates of a structure. PENSA represents each ensemble (e.g., simulation trajectory) by the same set of F features $\{x_1, \dots, x_F\}$. Here we discuss the types of features we consider most suited for a systematic analysis of molecular structure, currently including torsion angles, interatomic distances, water cavities and ion binding sites (for an overview, see Fig. 2). They are implemented in PENSA using MDAnalysis^{30,31} and PyEMMA³² and can be replaced or extended by other descriptions. PENSA is modular and new feature readers can be added easily.

Representing Molecules by Torsion Angles: Because the energy minima of molecular structures are largely determined by stereochemistry, the 3D conformation of most biological macromolecules can be approximately described using a set of torsion angles. For proteins, we use torsions around chemical bonds to describe the effective degrees of freedom in the protein backbone and the side chains (Figure 2). The three rotatable bonds in the protein backbone are characterized by angles ϕ , ψ , and ω . As ω is almost always in trans configuration, we only use ϕ and ψ . In addition, the amino acid side chains have up to five rotatable bonds. This re-

sults in a number of variables that grows linearly with the number of residues, describing the full protein structure while avoiding the redundancy that comes with using Cartesian coordinates (Fig. 2A). The analogous description of nucleic acids via torsion angles requires the definition of pseudo-torsions³³. The 3D structure of DNA or RNA can be described via the six main chain torsion angles (α , β , γ , δ , ϵ , ζ) around the covalent bonds and the angle χ about the glycosidic bond and the sugar pucker (Fig. 2B). An alternative description — also implemented in PENSA — uses two pseudo-torsions, η and θ , that are defined around imaginary lines connecting more distant atoms.³³

Representing Molecules by Distance: The set of all distances between all atoms provides a complete description of the structure of a molecule, independent of the coordinate system. However, taking into account all N atoms is extremely inefficient as the number of distances required grows $\propto N^2$ while the number of degrees of freedom grows $\propto N$. Reducing the set of distances to a few relevant ones can make this approach much more efficient. For example, the overall structure of a protein is usually described by the distances between all $C\alpha$ atoms. A further reduction in redundancy can be achieved by using system-specific knowledge, obtaining a subset that is smaller but still representative for the overall dynamics of the system. Common examples for this are hydrogen bond lengths to describe bonding patterns or base-pair distances in DNA. A combined analysis of distances and torsions can be beneficial as some effects can be easier to spot in distances and others in torsions.

Representing Water Cavities: We have implemented a new method to represent the presence and orientation of internal water molecules, which are crucial to the structure and function of many biomolecules. Typically, internal water molecules are defined by the protein sites they bind to, or by an atomic density that averages the motion of the waters.^{34–37} PENSA adds to this with a dynamic, orientation-based representation of water molecules in cavities within a biomolecule. Because water cavities are often accessible to water molecules in a freely diffusing bulk solvent, water molecules may interchange in a water cavity while maintaining the function of the cavity. Therefore, featurization of a certain water *site* within the biomolecule is more important than the individual water molecules that occupy the cavity. The polar nature of water molecules enables a water cavity to function as a polarizable interface, mediating hydrogen bond networks between amino acids that would otherwise be impossible to form. Any cavity that can accommodate a water molecule can additionally be unoccupied, whereby the occupation of the cavity can act as a further feature. To account for both of these effects, PENSA featurizes a wa-

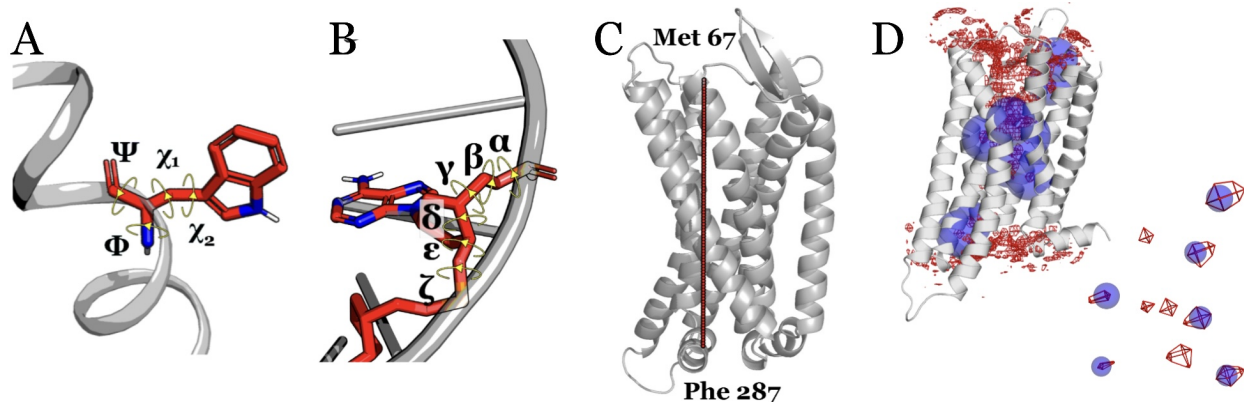


FIG. 2. Examples for biomolecular features implemented in PENSAs. *A*: Amino acid backbone torsion angles, Φ and Ψ represent amino acid backbone torsion angles, while χ_i represent amino acid side chain torsion angles, as depicted on Tryptophan. *B*: Representative angles for DNA and RNA. Six backbone-torsions sufficiently represent the torsional modes of DNA and RNA. *C*: Distances between backbone C- α 's of residue pairs in two G-protein coupled receptor ensembles. These distances represent divergences between ensembles in example study seen in section III C. *D*: Description of top 10 most probable water sites featurized from water density surrounding the protein accompanied with close up of featurization. Structures are visualized using PyMol²⁶ and density features using Biotite²⁷.

ter cavity via its occupation and, when occupied, the orientation of the water molecule. First, we locate the cavities by finding all local maxima within a 3D density grid. The grid is obtained by aligning the assembled trajectories such that the density refers to the combined ensemble and can be used to compare identical cavities across the ensembles. Each local maximum marks the center of a water cavity, defined as a sphere of radius 3.5 Å, based on hydrogen bonding interaction distances.³⁸ For each simulation frame, the cavity feature value is defined by the orientation of the water molecule (if occupied), or a value representing its unoccupied state. The water molecule's orientation is represented by the angular components of its dipole moment in spherical coordinates. This representation is appropriate when rotation, translation, and periodicity effects of the simulation system during the simulation are excluded from the water pocket featurization during preprocessing.

Representing Ion Cavities: PENSAs provides a similar approach to featurize ion cavities, which play important roles in the structure and function of many biomolecular systems — from ion channels to catalytic enzymes^{39,40}. Simulation trajectories must be preprocessed in the same manner as for water cavities, ensuring that the ion density grid is not affected by any system rotation, translation or switches between periodic boundaries. Ion cavities are then represented as a binary feature describing the presence or absence of an ion in the cavity, or as a discrete feature describing the ion indices that occupy the cavity, for instance in order to keep track of functionally relevant ion binding and unbinding events. This repre-

sentation allows for an investigation of the movement of specific ions in and out of an array of ion binding sites, and has already been employed to identify co-operative knock-on permeation of ions bound to different sites of cation channels.⁴¹

B. Feature Transformations

Multivariate Discretization: PENSAs offers an automatic discretization of one or multiple combined features into distinct states. For example, amino acid torsions typically oscillate about local minima in populations known as rotamers, often sampling different rotamers in an MD simulation.^{42–44} In the Dunbrack library,⁴³ each local rotamer can be accurately represented by a Gaussian distribution around the minimum energy conformation. Similarly, Gaussians can represent the oscillation of a water molecule's polarization (orientation of its dipole) within a water cavity, while cavity occupancy changes can be conveniently considered as two discrete populations with zero oscillation. The discrete states of these distributions are generated by applying a multi-modal Gaussian fit. The fit parameters are obtained with a non-linear least squares fit of up to ten Gaussians to each feature distribution using the SciPy library⁴⁵. For our purposes, we found this method to be computationally more efficient than alternative methods such as Gaussian Mixture Model. The state limits for each distribution are then defined by the Gaussian intersects. Distributions which have a cyclic periodicity may oscillate about a periodic

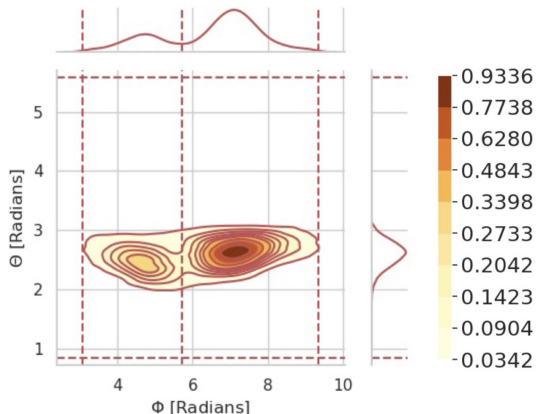


FIG. 3. Discrete macrostates of a water cavity generated by discretization of individual pairs of spherical coordinates (ϕ, θ) of the polar vector of each water molecule within the water cavity. Red dashed lines depict the state boundaries and include the periodic boundaries as the first and last state boundaries.

boundary but show up as two states on different ends of the distribution. To account for this boundary effect, all periodic distributions can be linearly shifted. In general, state limits can be defined for any kind of distribution, even non-Gaussian, using suitable clustering algorithms. For these cases, PENSA allows the manual input of arbitrary state boundaries. In instances where the dynamics of an amino acid are described by a combined view of all side-chain angles, e.g., the five side-chain torsions of arginine, an arbitrary number of N dimensions can be combined into one joint feature. The states of an N -dimensional feature are then the combination of all discretized microstates, defining a grid in the combined feature space, as shown in Fig. 3.

Dimensionality Reduction: Comparisons of multiple complex systems can be made more tractable by representing these systems in terms of low-dimensional, higher-order descriptions that summarize a large number of primary features in a small number of quantities. The most popular algorithm for such dimensionality reduction is Principal Component Analysis (PCA)⁴⁶. Time series, such as those from molecular dynamics simulations, can also be projected via Time-Lagged Independent Component Analysis (TICA)⁴⁷. Classically, dimensionality reduction has been applied on single ensembles. But to detect patterns across ensembles and differences between them, we have to define the same representation for all investigated ensembles. PENSA users can perform dimensionality reduction on the combined data of all ensembles included in the analysis and then compare them along the resulting reduced dimensions.

Clustering: The coordinate space defined by the dimensionality reduction methods discussed above can be clustered into discrete states, again using data from all ensembles. Clustering the structures from all ensembles in the resulting lower-dimensional space provides discrete states. PENSA implements k-means clustering⁴⁸ and regular-space clustering⁴⁹, two popular algorithms for this task. Users can calculate populations of the resulting discrete states in each ensemble and compare them.

C. Feature-by-Feature Comparison

The local extent of deviations between two ensembles can be quantified by comparing each feature's probability distribution in one ensemble to its distribution in the other ensemble. For a feature x_f in a simulation trajectory of length T , the T samples of x_f give an empirical estimation of the distribution $p(x_f)$, which describes the behaviour of x_f in that ensemble. We want to compare the distribution $p_i(x_f)$ in ensemble i to the corresponding distribution $p_j(x_f)$ in ensemble j . These distributions may have complex functional form, hence comparing their summary statistics (mean and standard deviation) might not be sufficient as they cannot capture more subtle differences in the distributions, e.g., the split-up of one state (unimodal distribution) into two states (bimodal). Instead, PENSA provides comparison measures that are designed to capture differences in probability distributions, namely the Jensen-Shannon Distance (JSD) and the Kolmogorov-Smirnov Statistic (KSS) divergence.

Jensen-Shannon Distance: Two distributions can be compared using the Jensen-Shannon distance D_{JS} , a symmetrized and numerically more stable version of the Kullback-Leibler divergence D_{KL} . For two distributions over a feature x_f from ensemble i and ensemble j , D_{JS} is defined below

$$D_{JS}[p_i||p_j] = \frac{1}{4} \sqrt{D_{KL}[p_j||\bar{p}] + D_{KL}[p_i||\bar{p}]} \quad (1)$$

$$\text{with } \bar{p} = \frac{p_i + p_j}{2}$$

with D_{KL} the Kullback-Leibler divergence. For numerical reasons, we always use its discrete version:

$$D_{KL}[p_i(x_f)||p_j(x_f)] = \int p_j(x_f) \log \frac{p_i(x_f)}{p_j(x_f)} dx \quad (2)$$

$$\approx \sum_{x_f \in \mathcal{X}_f} p_j(x_f) \log \frac{p_i(x_f)}{p_j(x_f)}$$

where \mathcal{X}_f is the set of possible states. In the case of continuous features, these states are bins along the fea-

ture coordinate, obtained by evenly dividing the range of the joint distribution. Note that D_{KL} is not symmetric, i.e., $D_{KL}[p_i \parallel p_j] \neq D_{KL}[p_j \parallel p_i]$ but D_{JS} is. The use of JSD as a comparison metric has been discussed in more detail in previous work¹⁷ where the comparison was performed on entire ensembles instead of individual features. Most importantly, in contrast to the unbounded — and in practice often divergent — KL divergence, the Jensen-Shannon distance ranges from 0 to 1 where 0 is obtained for identical distributions and 1 for a pair of completely different distributions.

Kolmogorov-Smirnov Statistic: Alternatively, we can quantify the differences between two distributions of continuous features without the need to define a binning parameter by using the Kolmogorov–Smirnov statistic D_{KS} . It is defined for a feature x_f as

$$D_{KS}(p_i \parallel p_j) = \sup_{x_f} \|F_{p_i}(x_f) - F_{p_j}(x_f)\| \quad (3)$$

with $F_{p_i}(x_f)$ and $F_{p_j}(x_f)$ the empirical distribution functions of $p_i(x_f)$ and $p_j(x_f)$, respectively. The empirical distribution functions are directly obtained from the calculated features and require no sorting of the data into arbitrary bins. The results of D_{JS} and D_{KS} for the same comparison ideally are very similar which can serve as an important sanity check.

Overall Ensemble Similarity: The overall similarity of two ensembles over all features in a metrics can be quantified by aggregating similarity metrics of all features x_f . For example, an average Kolmogorov-Smirnov statistic \bar{D}_{KS} of two ensembles i and j can be computed as:

$$\bar{D}_{KS} = \frac{1}{F} \sum_{f=1}^F D_{KS}[p_i(x_f) \parallel p_j(x_f)] \quad (4)$$

and \bar{D}_{JS} analogously. Aggregation functions other than the average, including the maximum and the minimum, are also implemented. Similar to other metrics that quantify the similarity of two ensembles in a single score,^{16–18} these aggregated metrics are particularly helpful when we need to evaluate the output of a new method to a reference ensemble, for example comparing a simulation or a generative machine learning model to a ground truth from an experiment or a more accurate level of simulation.

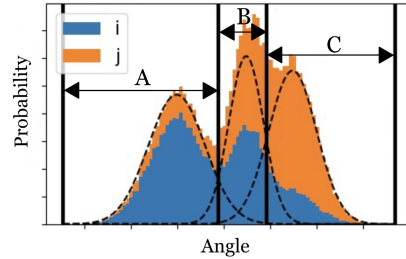
D. Mutual Information Analysis

A mutual information analysis can be employed to measure how much the specific value of one feature is coupled to the specific value of another.⁵⁰ Applying this approach to two conformational ensembles i and j , one

1. Combine data points for x_f across ensembles i and j

i0	i1	i2	i3	i4	i5	i6	i7	i8	i9	j0	j1	j2	j3	j4	j5	j6	j7	j8	j9
----	----	----	----	----	----	----	----	----	----	----	----	----	----	----	----	----	----	----	----

2. Discretize x_f histogram into states (A, B and C)



3. Transform data points into state IDs - $S(x_f)$

A	A	B	C	A	B	A	A	B	A	C	C	A	B	C	B	C	B	C	C
---	---	---	---	---	---	---	---	---	---	---	---	---	---	---	---	---	---	---	---

4. Combine feature states and ensemble states

Ai	Ai	Bi	Ci	Ai	Bi	Ai	Ai	Bi	Ai	Cj	Cj	Aj	Bj	Cj	Bj	Cj	Bj	Cj	Cj
----	----	----	----	----	----	----	----	----	----	----	----	----	----	----	----	----	----	----	----

FIG. 4. Schematic illustration of the calculation process for the State-Specific Information of feature x_f , $I_{SSI}(x_f)$. The combined data points for feature x_f are discretized into states defined by the intersects of a Gaussian fit to the data histogram; blue and orange represent ensembles i and j , respectively. Each data point is transformed into the corresponding discrete state it lies within ($S(x_f)$) and combined with the ensemble states - i or j . Colors are added to the data points on step 4 to highlight the unique substates that arise from the combination of feature states and ensemble states.

can identify if the specific values of a feature are dependent on the system ensemble - i or j , and *vice versa*, how much the value of a feature reveals about whether it stems from ensemble i or j . The ensemble identifiers i and j are then equivalent to the values of an additional feature within one (joint) ensemble. PENSA focuses on mutual information shared between a feature’s conformational states (e.g., the multivariate states described in section II B) and the ensemble states i and j . To quantify this, we calculate the State-Specific Information (SSI, Fig. 4), a linear, discrete-state adaptation of mutual information that has originally been developed for amino acid torsions that act as molecular switches⁸ but here is generalized to any feature with a distribution that can be represented as discrete states. It should be noted that an arbitrary number of ensembles could be incorporated into the SSI calculation, simultaneously measuring the mutual information between all conditions and a feature, but it is currently implemented for two. Similarly, SSI can operate on a single ensemble that is partitioned into two sub-ensembles, e.g., along a state boundary.

State-Specific Information (SSI): The SSI measure $I_{SSI}(x_f)$ quantifies the degree to which conformational state transitions of feature x_f signal information about

the ensembles i and j or the transitions between them. It is defined as

$$I_{SSI}(x_f) = \sum_{\substack{s \in S(x_f) \\ e \in [i, j]}} p(s, e) \log \frac{p(s, e)}{p(s)p(e)} \quad (5)$$

where $S(x_f)$ is the transformation of the combined data points of x_f across ensembles i and j into data points referring to a feature state-identifier s , derived from the discretized probability distribution of x_f , as seen in figure 4. The variable e is a generic representation of the ensemble ID, with possible values i or j . $p(s, e)$ is the joint distribution of a feature state of x_f and ensemble state (obtained from the probabilities of each element in the list shown in Fig. 4, step 4.), and $p(s)$ and $p(e)$ are the marginal distributions. The SSI ranges from 0 bits to 1 bit, where 0 bits represents no shared information and 1 bit represents maximal shared information between the ensemble (transitions) and the features.

State-Specific Co-Information (CoSSI): To quantify the degree to which two features interact with one another as they signal information about the ensemble they are in (i or j), State-Specific Co-Information (CoSSI) is employed. This multivariate feature-feature-ensemble metric is the linear, discrete-state adaptation of co-information⁵¹ that uses Shannon’s discrete entropy formulation⁵⁰, calculated using

$$\begin{aligned} I_{CoSSI}(x_1, x_2) &= \sum_{\substack{s_1 \in S(x_1) \\ s_2 \in S(x_2)}} p(s_1, s_2) \log \frac{p(s_1, s_2)}{p(s_1)p(s_2)} \\ &- \sum_{\substack{s_1 \in S(x_1) \\ s_2 \in S(x_2) \\ e \in [i, j]}} p(s_1, s_2, e) \log \frac{p(s_1, s_2, e)p(e)}{p(s_1, e)p(s_2, e)} \end{aligned} \quad (6)$$

where the transformation $S(x_f)$ is as previously defined. I_{CoSSI} can be positive or negative, indicating whether the switch between ensembles increases ($I_{CoSSI} > 0$), decreases ($I_{CoSSI} < 0$), or does not affect ($I_{CoSSI} = 0$) the communication between two features x_1 and x_2 . In the case of small-molecule ligand binding, for instance, positive I_{CoSSI} between features can represent the turning-on of a signal channel by a ligand.

E. Visualization

PENSA includes convenient functions to visualize all stages of the analysis workflow. Primary features as well

as processed features (like projections onto PCA eigenvectors) can easily be compared individually using histograms or inferred densities, and combinations of two features using heatmaps, with all functionality based on Matplotlib.⁵² The water and ion cavity featurizer writes out a structure file with the average position of the molecular ensemble, generated via MDAnalysis,³⁰ with additional atoms added via Biotite²⁷ that mark the cavity centers and store the magnitude of the probability maxima. Input structures can be sorted along the values of primary or processed features using MDAnalysis³⁰ which is particularly useful for PCA or tICA to see which component of a molecule’s motion is associated with which eigenvector. Analysis metrics for comparison and mutual information that are related to a single residue (e.g., the maximum JSD of all side-chain torsions in an amino acid) can be stored in structure files using MDAnalysis³⁰ and we provide scripts for PyMol²⁶ and VMD⁹ to visualize them via the color or the width of the cartoon representation. Metrics related to two features (e.g., distances) are visualized in square heatmaps, also implemented via Matplotlib.⁵² These visualization options provide a comprehensive overview of complex systems in one — or very few — figures.

III. EXAMPLE APPLICATIONS

A. Understanding effects of a small chemical modification: loop opening in an oxidoreductase

As a first example, we show how the systematic comparison of protein backbone and side-chain torsions provides a comprehensive overview on the differences in the conformational ensembles induced by a small chemical modification. We consider the oxidation of two cysteine thiols to a disulfide bond in the N-terminal domain of the key bacterial oxidoreductase DsbD (nDsbD). DsbD plays an important role in electron transport across the inner cytoplasmic membrane of gram-negative bacteria and this reaction is an important step in its catalytic cycle.²⁸

Visualization of the maximum JSD per residue for backbone and sidechain torsions (see Fig. 5) shows at once the opposing residues in the gap loop to be the most affected regions. Unsurprisingly, the residues directly involved in the reaction, Cys103 and Cys109, show the highest values. The effects of this reaction on the surrounding residues – showing up in our analysis as medium JSD values – cause a change in the distance of the opposing loop and a corresponding opening of the gap. In particular, we find residues Phe70 and Tyr71 at the neighboring loop to be strongly affected. Indeed, the

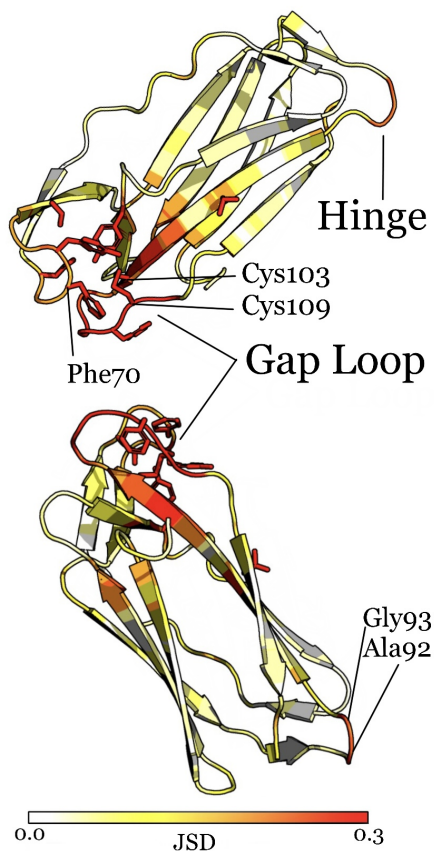


FIG. 5. Comparison of torsion angles via the Jensen-Shannon Distance (JSD) reveals where conformational ensembles differ and allows to visualize these effects on a single structure. Analysis of backbone and side-chain torsions highlights regions of nDsbD that are most affected by the oxidation of the two cysteine thiols, Cys103 and Cys109²⁸. For each residue, the maximum JSD of the distributions of backbone torsion angles between oxidised and reduced condition is encoded in the color of the cartoon representation from white (0.0) via yellow and orange to red (0.3). Similarly, the maximum JSD for the sidechain torsion angles is encoded in the color of the side chains, where stick representation of side chains is only displayed for residues with JSD values greater than 0.3. Structures are visualized using PyMol.²⁶

authors of the original study identified the distance between residues Phe70 and Cys109 to be the characteristic hallmark of loop opening.

Besides the influence on the gap loop, we identify a more subtly involved and previously not discussed region at the opposite side of the protein. This region – mainly the backbones of residues Ala92 and Gly93 – functions as a hinge for the beta-strand region that slightly tilts when the gap loop is pushed outward during the gap opening.

This finding demonstrates how our approach picks up differences between simulations that are otherwise easily missed.

B. Comparing force field parameters: Interactions of Calcium with DNA

As a second use case, we show how to quantify the effects of small changes in force field parameters on the overall conformational ensemble (Fig. 6). We consider the binding of calcium ions (Ca^{2+}) to DNA²⁹. Metal cations play a crucial role in stabilizing the structure of nucleic acid systems. Their force field parameters are usually determined to reproduce bulk properties like the solvation-free energy and thus often not directly transferable to interactions with biomolecules.⁵³ Furthermore, small changes in the interactions can have significant conformational consequences overall.⁵⁴ Studying the effect of such small changes on the overall conformation is an important problem in force field optimization.

Comparison of DNA backbone torsions from MD simulations using the standard force field parameters for Ca^{2+} -DNA interactions to an experimental reference ensemble reveals a periodic pattern of strong deviations along the entire double strand that are strongly reduced by using optimized force field parameters. We generate the reference distribution from the experimental structure by Gaussian sampling of the relevant coordinates using the uncertainty of the X-ray structure (1.7 Å, PDB: 477D) as the width of the distribution. We then compare the simulations of each parameter set to this reference (Fig. 6) using the Kolmogorov-Smirnov statistic (Eq. 3) because it provides a parameter-free measure for the deviations. The approximate periodicity of the deviations (Fig. 6, left) shows that, using standard parameters, the conformational ensemble as a whole deviates from the reference distribution and has problems reproducing the overall structure of the double strand. The authors of the original study²⁹ identified an overestimation of Ca^{2+} -DNA interactions as the main cause of such deviations. It allows the Ca^{2+} ions to bridge between the phosphate oxygen atoms of opposite backbone strands which causes the minor groove of the DNA strand to shrink and in turn affects the entire structure. Thus, they rescaled the force field parameters to optimize the Ca^{2+} -DNA interactions. This not only improved the local accuracy but the entire conformational ensemble, even though the overall structure was not explicitly optimized for during the rescaling. In our PEnSA-based analysis, this improvement is immediately visible by the reduced deviations (Fig. 6, right). The overall ensemble KSS (as in Eq. 4) is reduced from 0.50 (standard force field) to



FIG. 6. Comparison of torsion angles via the Kolmogorov-Smirnov Statistic (KSS) reveals where conformational ensembles differ and allows to visualize these effects on a single structure. Comparison of DNA backbone torsion angles from MD simulations to an experimental reference ensemble (see main text for details) shows the improvement in the ensemble generated by MD simulations when switching from standard force field parameters (left) to optimized force field parameters (right). Structures are visualized using PyMol.²⁶

0.34 (optimized force field). This example shows that our workflow quickly identifies whether and where small changes in local interactions propagate to strong deviations in the overall structure of a biomolecule.

C. Tracing information linked to a protonation state: The central aspartic acid in the μ -opioid receptor

To showcase the usefulness of State-Specific Information (SSI), we investigate the relationship between the protonation state of a central aspartic acid and the μ -opioid re-

ceptor (μ OR) ensemble. The μ OR, a G protein-coupled receptor (GPCR), is a transmembrane receptor protein that converts extracellular stimuli into intracellular signalling cascades. The diversity in structure and function among GPCRs underpins complex activation mechanisms that, despite large pharmaceutical interest, remain unresolved.^{55–57} Rotamer changes in residue side chains give rise to larger-scale conformational changes that enable the binding of effector proteins and trigger downstream signaling (receptor activation).⁵⁸ These rotamers can be understood as molecular micro-switches, making them an ideal use case for our state-based mutual information approach, SSI. Many receptors are influenced by environmental pH changes,^{59–61} and protonation changes of an evolutionarily conserved aspartic acid residue have been hypothesised to represent a key step in receptor activation.^{62–64} Here, we apply SSI to side-chain and backbone torsions to investigate the effect of protonating this conserved aspartic acid, Asp114 (i = protonated, j = de-protonated) in the antagonist-bound μ OR (PDB: 4DKL, Fig. 7).

Mutual information analysis of side-chain rotamers: The SSI values calculated for each residue reveal those parts of the receptor that signal information about the protonation state of Asp114 (Fig. 7). Namely, rotameric state changes in the backbone torsions of transmembrane helix TM6, proximal to Asp114, are coupled to the protonation state changes of Asp114. Similarly, the backbone rotamer states of intracellular loops ICL2 and ICL3 couple to the protonation state of Asp114. An outward swing of TM6, enabled by backbone conformational state changes near Phe289 (P-I-F motif), is characteristic of receptor activation,⁵⁵ and specific conformations of ICL2 and ICL3 are implicated in the binding of signal proteins.^{65,66} Furthermore, side chain changes are identified on the P-I-F motif, the NPxxY motif, and the DRY motif, three receptor motifs that are known to undergo distinct rotamer changes in the transition from inactive to active receptor states.⁵⁵ The recognition of receptor regions where conformational changes are associated with activation and signaling suggests that the Asp114 protonation state and GPCR activation are intertwined. This example thus demonstrates how SSI and its visualization help to pinpoint receptor regions where the features' rotamer states inform about an aspartic acid's protonation state.

Mutual information analysis of intracavity water sites: To further demonstrate how SSI can be used to analyze water cavity features, we featurized the ten most well-defined water sites (Fig. 7). The locations of the water cavities were determined using the PENSEA water featurizer as the ten sites with the largest probability maxima in the water density grid of the combined ensembles and labelled O1–O10 according to their ranking. The posi-

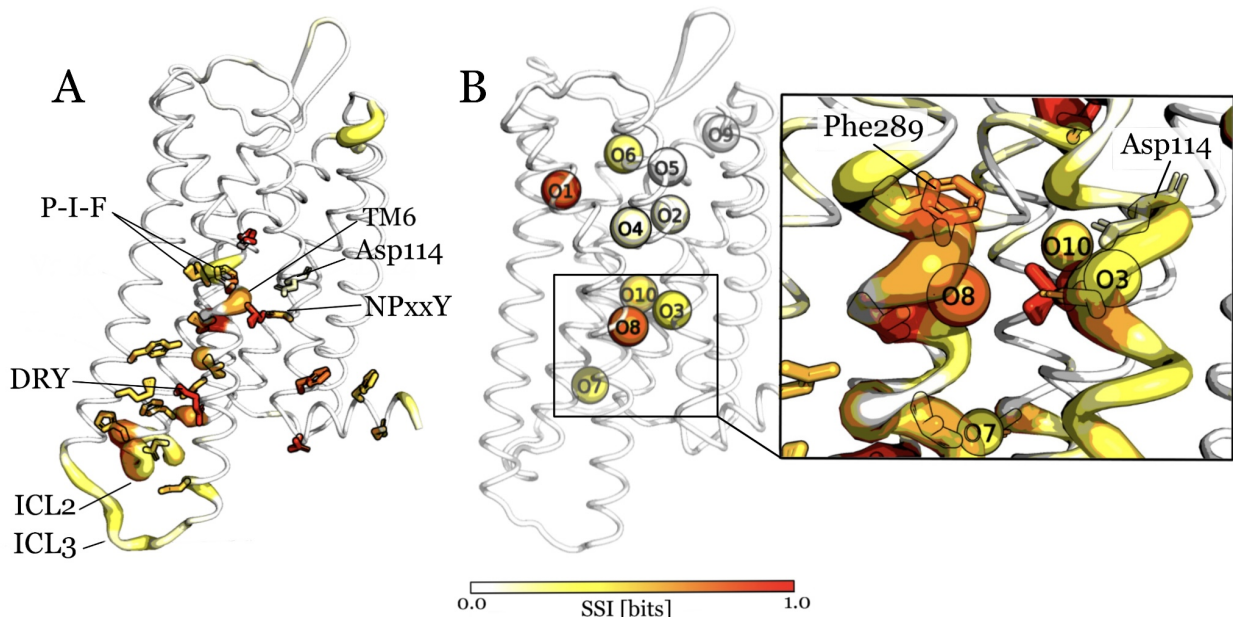


FIG. 7. Analysis of backbone and side-chain torsion angles (A, cartoon and stick), and intracavity water molecules (B, spheres), via State-Specific Information (SSI) quantifies the information that each feature signals about the protonation state of Asp114 in the μ -opioid receptor. SSI highlights that changes in the protonation state of Asp114 couple to rotameric state changes on: the backbone of TM6, proximal to Asp114; the backbone of ICL2 and ICL3; residue side chains on the P-I-F, NPxxY and DRY motifs; and water sites distributed throughout the receptor. The SSI for backbone torsions is encoded in the color and width of the cartoon representation from white (0.0), via yellow (0.33) and orange (0.67), to red (1.0). Similarly, the SSI for sidechain torsions is encoded in the color of the stick representation, and for intracavity water sites in the color of the sphere representation. For ease of visualization, only side chains corresponding to the twenty largest SSI values are displayed and backbone torsions are represented solely by cartoon. The right panel shows a close-up view of the region proximal to Asp114, with SSI values for backbone and side chains projected onto the receptor in the same manner as in panel A. Structures are visualized using PyMol.²⁶

tioning of all ten sites agrees well with water molecules resolved in experiments^{67,68} and predicted by the HomWat server⁶⁹ for the inactive μ OR crystal structure (PDB: 4DKL), confirming the accuracy of PENSEA's water cavity featurization. Three water cavities are within the vicinity of Asp114: O3, O8 and O10. Using SSI (eq. 5), we calculated that water cavities O1–O10 share information with the Asp 114 protonation state on levels between 0.00–0.74 bits. Water cavity O8, for example, shares 0.67 bits of information in coupled conformational state changes linked to the transition between ensemble i and j , i.e., unprotonated to protonated Asp114. O8 also sits beside Phe289 of the P-I-F motif, where we identified that backbone rotamer state changes are coupled to Asp114 protonation. Surprisingly, the more distant water site O1 shares 0.74 bits of information, 82% of which is due to an occupancy change. Comparing the average ensemble structures reveals an increased packing between TM5 and TM6 in the region about the water O1 cavity, with the distance between surrounding C α s moving over on average 1Å closer in the Asp114-protonated

ensemble, suggesting that helix movements on TM6 lead to a collapse of the cavity. This analysis highlights a concerted behaviour of water cavities and TM6, whereby state changes to both are indicative of the protonation state of Asp114. It shows how the combined analysis of multiple different features and a comprehensive visualization help to find interrelations within a receptor and discover signaling pathways.

IV. DISCUSSION

With PENSEA, we have implemented an open-source library that provides systematic, easy-to-apply methods that make the otherwise often cumbersome exploration of biomolecular systems faster, more reliable and easier to interpret. The data readers implemented in PENSEA engage with a range of biomolecular systems via robust featurization implementations. These include readers for interatomic distances and the characteristic torsion angles of amino acids and nucleic acids as well as a novel

approach that reliably incorporates water and ion cavities via their occupancy and, in the case of water, the polarization of the cavity. Combined with dimensionality reduction tools, PENSA can handle biomolecular systems on a wide range of scales and resolutions. PENSA includes two comparison measures with slightly different use cases: JSD is a fast way to compare ensembles and pick up relevant features. The sensitivity of JSD depends on — and can be adjusted via — the spacing of the discretization. KSS is a parameter-free metric that picks up every ensemble difference, even the noise. In most practical cases, JSD and KSS provide similar results. In addition, PENSA includes a mutual information measure, State-Specific information (SSI). With no prior knowledge of the data, PENSA performs an automatic discretization of feature distributions into conformational states, and via SSI, quantifies the information that each features’ conformational states signal about the ensemble they are in. The ideal use case involves features that switch between well-defined states, such as molecular switches, however customizable state definitions allow SSI to operate with many kinds of feature discretization. SSI can be further extended to three or more features to quantify information flow within a system but is currently only implemented for two. Combined with PENSA’s convenient visualization tools, these methods allow for a detailed analysis of biomolecular ensembles without the bias of hand-picked metrics, acting as a solid basis for mechanistical interpretations and further, more detailed analysis.

Our example analyses demonstrate the versatility of PENSA on three different biomolecular systems. By investigating the effects of a small chemical modification on loop opening in an oxidoreductase with JSD, we demonstrate the validity of the method in confirming previously discovered results, while additionally reporting novel, more subtle findings within the same system. We demonstrate the applicability of PENSA in the optimization of force field parameters via a comparison of the interactions between Calcium and DNA under different force field parameters with KSS. Finally, we report on a communication channel in the μ -opioid receptor that transmits information between the intracellular signalling site and the protonation state of a distal aspartic acid, shedding further light on the signal transduction mechanism of this mechanistically complicated system. The major limit to the accuracy of PENSA is the quality of the input ensembles. For example, insufficiently converged MD simulations can cause false positives when an equally probable transition happens only in one of the conditions. Or they can cause false negatives for overall rare events or slow processes. If in doubt, validation by other means may be necessary (experiment, in-

dependent/longer simulations). Although non-converged simulations can give useful hints, these cases demand a cautious systematic analysis. Despite these caveats, PENSA has the potential for high-throughput analysis of a large amount of simulations, e.g., those available in GPCRmd⁷⁰, can be used to independently quantify the quality of force fields or generative machine learning models, and unravel molecular mechanisms and signaling pathways.

V. CONCLUSIONS

In summary, we present a powerful toolkit to build workflows for the systematic and quantitative analysis of biomolecular systems and their conformational ensembles. PENSA provides flexible options to featurize various biomolecular systems, metrics to compare ensembles and to detect interrelations between different regions of a system, and methods to produce intuitive visualizations. We demonstrate the effectiveness of these methods on three real-world examples from molecular biology, showing how PENSA makes it easier for researchers to analyze large amounts of complex simulation data.

VI. ACKNOWLEDGMENTS

We thank Lukas Stelzl for the trajectory data of the oxidoreductase example as well as Sergio Cruz-León, Kara Grotz, and Nadine Schwierz for the trajectory data of the DNA-Calcium example. We are grateful to Alexander Powers, Lukas Stelzl, Nicole Ong, Eleanore Ocana, Emma Andrick, Callum Ives, and Bu Tran for beta-testing as well as Maria Karelina, Marc Dämgen, Patricia Suriana, Sergio Cruz-León, Michael Ward, and Ramon Guixà-González for helpful discussions. M.V. was supported by the EMBO long-term fellowship ALTF 235-2019. N.J.T. was supported by a BBSRC EASTBIO PhD studentship. This work was supported by National Institutes of Health grant R01GM127359 (R.O.D.) An award of computer time was provided by the INCITE program. This research used resources of the Oak Ridge Leadership Computing Facility, a DOE Office of Science User Facility supported under contract DE-AC05-00OR22725. Additional computing for this project was performed on the Sherlock cluster and the University of Dundee SLS HPC cluster. We thank Stanford University, the Stanford Research Computing Facility, and the University of Dundee for providing computational resources and support that contributed to these research results.

- ¹S. A. Hollingsworth and R. O. Dror, *Neuron* **99**, 1129 (2018).
- ²C. R. Knoverek, G. K. Amarasinghe, and G. R. Bowman, *Trends in Biochemical Sciences* **44**, 351 (2018).
- ³C.-M. Suomivuori, N. R. Latorraca, L. M. Wingler, S. Eismann, M. C. King, A. L. W. Kleinhenz, M. A. Skiba, D. P. Staus, A. C. Kruse, R. J. Lefkowitz, and R. O. Dror, *Science* **367**, 881 (2020).
- ⁴D. Provasi, M. C. Artacho, A. Negri, J. C. Mobarec, and M. Filizola, *PLoS Computational Biology* **7**, 1 (2011).
- ⁵J. D. McCorvy, K. V. Butler, B. Kelly, K. Rechsteiner, J. Karpiak, R. M. Betz, B. L. Kormos, B. K. Shoichet, R. O. Dror, J. Jin, and B. L. Roth, *Nature Chemical Biology* **14**, 126 (2018).
- ⁶J. F. Cordero-Morales, V. Jogini, A. Lewis, V. Vásquez, D. M. Cortes, B. Roux, and E. Perozo, *Nature Structural and Molecular Biology* **14**, 1062 (2007).
- ⁷Y. Liu, M. Ke, and H. Gong, *Biophysical Journal* **109**, 542 (2015).
- ⁸N. J. Thomson, O. N. Vickery, C. M. Ives, and U. Zachariae, *bioRxiv* (2021), 10.1101/2020.08.28.271510.
- ⁹W. Humphrey, A. Dalke, and K. Schulten, *Journal of Molecular Graphics* **14**, 33 (1996).
- ¹⁰W. L. DeLano, *CCP4 Newsletter on protein crystallography* **40**, 82 (2002).
- ¹¹R. O. Dror, D. H. Arlow, P. Maragakis, T. J. Mildorf, A. C. Pan, H. Xu, D. W. Borhani, and D. E. Shaw, *Proceedings of the National Academy of Sciences of the United States of America* **108**, 18684 (2011).
- ¹²Q. Zhou, D.-H. Yang, M. Wu, Y. Guo, W. Guo, L. Zhong, X. Cai, A. Dai, W. Jang, E. I. Shakhovich, Z.-J. Liu, R. C. Stevens, N. A. Lambert, M. M. Babu, M.-W. Wang, and S. Zhao, *eLife* **8**, e50279 (2019).
- ¹³R. O. Dror, H. F. Green, C. Valant, D. W. Borhani, J. R. Valcourt, A. C. Pan, D. H. Arlow, M. Canals, J. R. Lane, R. Rahmani, J. B. Baell, P. M. Sexton, A. Christopoulos, and D. E. Shaw, *Nature* **503**, 295 (2013).
- ¹⁴G. R. Bowman, E. R. Bolin, K. M. Hart, B. C. Maguire, and S. Marqusee, *Proceedings of the National Academy of Sciences of the United States of America* **112**, 2734 (2015).
- ¹⁵S. Zivanovic, G. Bayarri, F. Colizzi, D. Moreno, J. L. Gelpí, R. Soliva, A. Hospital, and M. Orozco, *Journal of Chemical Theory and Computation* **16**, 6586 (2020).
- ¹⁶R. Brüschweiler, *Proteins: Structure, Function and Genetics* **50**, 26 (2003).
- ¹⁷K. Lindorff-Larsen and J. Ferkinghoff-Borg, *PLOS ONE* **4**, 1 (2009).
- ¹⁸M. Tiberti, E. Papaleo, T. Bengtson, W. Boomsma, and K. Lindorff-Larsen, *PLoS Computational Biology* **11**, 1 (2015).
- ¹⁹F. Noé, S. Olsson, J. Köhler, and H. Wu, *Science* **365**, eaaw1147 (2019).
- ²⁰B. E. Husic and V. S. Pande, *Journal of the American Chemical Society* **140**, 2386 (2018).
- ²¹F. Nüske, H. Wu, J. H. Prinz, C. Wehmeyer, C. Clementi, and F. Noé, *Journal of Chemical Physics* **146**, 094104 (2017).
- ²²D. Fracalvieri, A. Pandini, F. Stella, and L. Bonati, *BMC Bioinformatics* **12**, 158 (2011).
- ²³M. D. Ward, M. I. Zimmerman, A. Meller, M. Chung, S. J. Swamidass, and G. R. Bowman, *Nature Communications* **12**, 1 (2021).
- ²⁴M. Malik, M. D. Ward, Y. Fang, J. R. Porter, M. I. Zimmerman, T. Koelblen, M. Roh, A. I. Frolova, T. P. Burris, G. R. Bowman, P. I. Imoukhuede, and S. K. England, *ACS Pharmacology and Translational Science* **4**, 1543 (2021).
- ²⁵M. Vögele, N. Thomson, S. Truong, and J. McAvity, "PENZA," (2021), doi: 10.5281/ZENODO.4362136.
- ²⁶Schrödinger, LLC, "The PyMOL molecular graphics system, version 1.8," (2015).
- ²⁷P. Kunzmann and K. Hamacher, *BMC Bioinformatics* **19**, 346 (2018).
- ²⁸L. S. Stelzl, D. A. Mavridou, E. Saridakis, D. Gonzalez, A. J. Baldwin, S. J. Ferguson, M. S. Sansom, and C. Redfield, *eLife* **9**, 1 (2020).
- ²⁹S. Cruz-León, K. K. Grotz, and N. Schwierz, *Journal of Chemical Physics* **154**, 171102 (2021).
- ³⁰N. Michaud-Agrawal, E. J. Denning, T. B. Woolf, and O. Beckstein, *Journal of Computational Chemistry* **32**, 2319 (2011).
- ³¹R. J. Gowers, M. Linke, J. Barnoud, T. J. E. Reddy, M. N. Melo, S. L. Seyler, J. Domański, D. L. Dotson, S. Buchoux, I. M. Kenney, and O. Beckstein, in *Proceedings of the 15th Python in Science Conference* (2016) pp. 98–105.
- ³²M. K. Scherer, B. Trendelkamp-Schroer, F. Paul, G. Pérez-Hernández, M. Hoffmann, N. Plattner, C. Wehmeyer, J. H. Prinz, and F. Noé, *Journal of Chemical Theory and Computation* **11**, 5525 (2015).
- ³³K. S. Keating, E. L. Humphris, and A. M. Pyle, *Quarterly Reviews of Biophysics* **44**, 433 (2011).
- ³⁴A. J. Venkatakrisnan, A. K. Ma, R. Fonseca, N. R. Latorraca, B. Kelly, R. M. Betz, C. Asawa, B. K. Kobilka, and R. O. Dror, *Proceedings of the National Academy of Sciences of the United States of America* **116**, 3288 (2019).
- ³⁵S. Yuan, S. Filipek, K. Palczewski, and H. Vogel, *Nature Communications* **5**, 4733 (2014).
- ³⁶L. Pardo, X. Deupi, N. Dölker, M. L. López-Rodríguez, and M. Campillo, *ChemBioChem* **8**, 19 (2007).
- ³⁷Y. Levy and J. N. Onuchic, *Proceedings of the National Academy of Sciences of the United States of America* **101**, 3325 (2004).
- ³⁸T. Kajander, P. C. Kahn, S. H. Passila, D. C. Cohen, L. Lehtiö, W. Adolfsen, J. Warwicker, U. Schell, and A. Goldman, *Structure* **8**, 1203 (2000).
- ³⁹B. Zarzycka, S. A. Zaidi, B. L. Roth, and V. Katritch, *Pharmacological Reviews* **71**, 571 (2019).
- ⁴⁰C. Andreini, I. Bertini, G. Cavallaro, G. L. Holliday, and J. M. Thornton, *Journal of Biological Inorganic Chemistry* **13**, 1205 (2008).
- ⁴¹C. M. Ives, N. J. Thomson, and U. Zachariae, *bioRxiv* (2022), 10.1101/2022.04.01.486690.
- ⁴²R. L. Dunbrack, *Current Opinion in Structural Biology* **12**, 431 (2002).
- ⁴³R. L. Dunbrack and M. Karplus, *Journal of Molecular Biology* **230**, 543 (1993).
- ⁴⁴A. D. Scouras and V. Daggett, *Protein Science* **20**, 341 (2011).
- ⁴⁵P. Virtanen, R. Gommers, T. E. Oliphant, M. Haberland, T. Reddy, D. Cournapeau, E. Burovski, P. Peterson, W. Weckesser, J. Bright, S. J. van der Walt, M. Brett, J. Wilson, K. J. Millman, N. Mayorov, A. R. J. Nelson, E. Jones, R. Kern, E. Larson, C. J. Carey, Í. Polat, Y. Feng, E. W. Moore, J. VanderPlas, D. Laxalde, J. Perktold, R. Cimrman, I. Henriksen, E. A. Quintero, C. R. Harris, A. M. Archibald, A. H. Ribeiro, F. Pedregosa, P. van Mulbregt, and SciPy 1.0 Contributors, *Nature Methods* **17**, 261 (2020).
- ⁴⁶K. P. F.R.S., *The London, Edinburgh, and Dublin Philosophical Magazine and Journal of Science* **2**, 559 (1901).
- ⁴⁷S. Schultze and H. Grubmüller, *Journal of Chemical Theory and Computation* **17**, 5766 (2021).
- ⁴⁸J. Macqueen, in *In 5-th Berkeley Symposium on Mathematical Statistics and Probability* (1967) pp. 281–297.
- ⁴⁹J.-H. Prinz, H. Wu, M. Sarich, B. Keller, M. Senne, M. Held, J. D. Chodera, C. Schütte, and F. Noé, *The Journal of Chemical Physics* **134**, 174105 (2011).
- ⁵⁰C. E. Shannon, *Bell System Technical Journal* **27**, 379 (1948).
- ⁵¹A. J. Bell, *4th International Symposium on Independent Component Analysis and Blind Source Separation* (2003).
- ⁵²J. D. Hunter, *Computing in Science and Engineering* **9**, 90 (2007).
- ⁵³M. T. Panteva, G. M. Giambaşu, and D. M. York, *Journal of Physical Chemistry B* **119**, 15460 (2015).
- ⁵⁴J. Yoo and A. Aksimentiev, *Journal of Physical Chemistry Letters* **3**, 45 (2012).

- ⁵⁵V. Katritch, V. Cherezov, and R. C. Stevens, *Annual Review of Pharmacology and Toxicology* **53**, 531 (2013).
- ⁵⁶A. S. Hauser, S. Chavali, I. Masuho, L. J. Jahn, K. A. Martemyanov, D. E. Gloriam, and M. M. Babu, *Cell* **172**, 41 (2018).
- ⁵⁷D. S. Eiger, U. Pham, J. Gardner, C. Hicks, and S. Rajagopal, *American Journal of Physiology-Cell Physiology* **322**, C887 (2022).
- ⁵⁸A. S. Hauser, A. J. Kooistra, C. Munk, F. M. Heydenreich, D. B. Veprintsev, M. Bouvier, M. M. Babu, and D. E. Gloriam, *Nature Structural and Molecular Biology* **28**, 879 (2021).
- ⁵⁹M. G. Ludwig, M. Vanek, D. Guerini, J. A. Gasser, C. E. Jones, U. Junker, H. Hofstetter, R. M. Wolf, and K. Seuwen, *Nature* **425**, 93 (2003).
- ⁶⁰J. B. Rowe, N. J. Kapolka, G. J. Taghon, W. M. Morgan, and D. G. Isom, *Journal of Biological Chemistry* **296**, 100167 (2021).
- ⁶¹E. J. Sanderlin, C. R. Justus, E. A. Krewson, and L. V. Yang, *Cell Health and Cytoskeleton* **7**, 99 (2015).
- ⁶²P. Ghanouni, H. Schambye, R. Seifert, T. W. Lee, S. G. Rasmussen, U. Gether, and B. K. Kobilka, *Journal of Biological Chemistry* **275**, 3121 (2000).
- ⁶³M. Mahalingam, K. Martínez-Mayorga, M. F. Brown, and R. Vogel, *Proceedings of the National Academy of Sciences of the United States of America* **105**, 17795 (2008).
- ⁶⁴O. N. Vickery, C. A. Carvalheda, S. A. Zaidi, A. V. Pislakov, V. Katritch, and U. Zachariae, *Structure* **26**, 171 (2018).
- ⁶⁵A. Koehl, H. Hu, S. Maeda, Y. Zhang, Q. Qu, J. M. Paggi, N. R. Latorraca, D. Hilger, R. Dawson, H. Matile, G. F. X. Schertler, S. Granier, W. I. Weis, R. O. Dror, A. Manglik, G. Skiniotis, B. K. Kobilka, C. J. Draper-Joyce, M. Khoshouei, D. M. Thal, Y.-L. Liang, A. T. N. Nguyen, S. G. B. Furness, H. Venugopal, J.-A. Baltos, J. M. Plitzko, R. Danev, and W. Baumeister, *Nature* , 547–552 (2018).
- ⁶⁶A. Mafi, S. K. Kim, and W. A. Goddard, *Proceedings of the National Academy of Sciences of the United States of America* **117**, 16346 (2020).
- ⁶⁷S. Granier, A. Manglik, A. C. Kruse, T. S. Kobilka, F. S. Thian, W. I. Weis, B. K. Kobilka, J. M. Mathiesen, R. K. Sunahara, and L. Pardo, *Nature* **485**, 321–326 (2012).
- ⁶⁸W. Huang, A. Manglik, A. J. Venkatakrishnan, T. Laeremans, E. N. Feinberg, A. L. Sanborn, H. E. Kato, K. E. Livingston, T. S. Thorsen, R. C. Kling, S. Granier, P. Gmeiner, S. M. Husbands, J. R. Traynor, W. I. Weis, J. Steyaert, R. O. Dror, and B. K. Kobilka, *Nature*, *Nature* **584**, E16 (2020).
- ⁶⁹E. Mayol, A. Garcia-Recio, J. K. Tiemann, P. W. Hildebrand, R. Guixa-Gonzalez, M. Olivella, and A. Cordomi, *Nucleic Acids Research* **48**, W54 (2020).
- ⁷⁰I. Rodríguez-Espigares, M. Torrens-Fontanals, J. K. Tiemann, D. Aranda-García, J. M. Ramírez-Anguita, T. M. Stepniewski, N. Worp, A. Varela-Rial, A. Morales-Pastor, B. Medel-Lacruz, G. Pándy-Szekeres, E. Mayol, T. Giorgino, J. Carlsson, X. Dupui, S. Filipek, M. Filizola, J. C. Gómez-Tamayo, A. Gonzalez, H. Gutiérrez-de Terán, M. Jiménez-Rosés, W. Jespers, J. Kapla, G. Khelashvili, P. Kolb, D. Latek, M. Marti-Solano, P. Matricon, M. T. Matsoukas, P. Miszta, M. Olivella, L. Perez-Benito, D. Provasi, S. Ríos, I. R. Torrecillas, J. Sallander, A. Szttyler, S. Vasile, H. Weinstein, U. Zachariae, P. W. Hildebrand, G. De Fabritiis, F. Sanz, D. E. Gloriam, A. Cordomi, R. Guixà-González, and J. Selent, *Nature Methods* **17**, 777 (2020).